JOURNAL OF GEOPHYSICAL RESEARCH, VOL. 112, E08S02, doi:10.1029/2006JE002840, 2007

Martian surface mineralogy from Observatoire pour la Minéralogie, l'Eau, les Glaces et l'Activité on board the Mars Express spacecraft (OMEGA/MEx): Global mineral maps

F. Poulet,[1] C. Gomez,[1] J.-P. Bibring,[1] Y. Langevin,[1] B. Gondet,[1] P. Pinet,[2] G. Belluci,[3] and J. Mustard[4]

Received 6 October 2006; revised 4 January 2007; accepted 1 May 2007; published 18 July 2007.

[1] After 2 years of operation the Observatoire pour la Minéralogie, l'Eau, les Glaces et l'Activité (OMEGA) imaging spectrometer on board Mars Express has acquired data coverage of the Martian surface with spatial resolution varying between 300 m and 4.8 km, depending on the pericenter altitude of the spacecraft's elliptical orbit. We report the global surface distributions of some minerals using the OMEGA observations in the visible and near infrared (VNIR) wavelength domains (0.35–2.5 μm). Global maps of ferric phases, mafic minerals (pyroxenes and olivines), and hydrated minerals have been derived from spectral parameters. The limits of detection in terms of abundance for some minerals of different grain size distributions are given. The distribution of pyroxenes is in general agreement with the mineral maps of previous telescopic and space observations. The Fe^{3+} absorption feature in the visible wavelength region is present everywhere on the surface. The spectra of the bright regions compare with anhydrous nanophase ferric oxides. Terrains with water-bearing minerals cover a very small fraction of the Martian surface. Olivine (Mg-rich compositions) is detected in more extensive regions of the pyroxene-rich zones than previously reported. Olivine with higher iron content and/or larger grain size (>100 μm) is only detected in isolated areas. The mineralogy of the northern low-albedo regions is discussed in the light of these mineral maps. Chemical alteration or oxidation during extrusion producing a coating or varnish of anhydrous ferric phases over a dark basaltic surface best accounts for the VNIR spectral properties of these regions, although a glassy composition resulting from impact is also considered.

Citation: Poulet, F., C. Gomez, J.-P. Bibring, Y. Langevin, B. Gondet, P. Pinet, G. Belluci, and J. Mustard (2007), Martian surface mineralogy from Observatoire pour la Minéralogie, l'Eau, les Glaces et l'Activité on board the Mars Express spacecraft (OMEGA/MEx): Global mineral maps, *J. Geophys. Res.*, *112*, E08S02, doi:10.1029/2006JE002840.

1. Introduction

[2] The Observatoire pour la Minéralogie, l'Eau, les Glaces et l'Activité (OMEGA) investigation is designed to study the surface and the atmosphere of Mars by coupling compositional measurements through visible and near infrared (VNIR) spectroscopy to imagery. The OMEGA instrument started its operation on January 2004, and achieved its prime objective over the nominal (1 Martian year) mission: to locate and map several key minerals of major importance to trace Mars evolution [*Arvidson et al.*, 2005; *Bibring et al.*, 2005, 2006; *Gendrin et al.*, 2005; *Langevin et al.*, 2005a; *Poulet et al.*, 2005].

[3] A global map produced from the OMEGA data will provide a more complete and planetary view of the Martian materials. In this study, we summarize the global distributions of Martian surface materials based on 1 Martian year of observation. This summary complements previous and ongoing efforts that focused on regional distribution of materials based on their spectral signatures. These investigations are presented in several other papers that reveal unique regional mineralogical units (e.g., phyllosilicates in Mawrth Vallis and olivine/phyllosilicate in Nili Fossae).

2. Previous Works

[4] Telescopic observations and early Mars space missions gave initial insights into the global surface composition of Mars (see, e.g., *Bandfield* [2002] and *Yen et al.* [2005] for recent reviews). Significant high-calcium pyroxene absorption bands in the low-albedo regions have been detected, while the high-albedo regions are spectrally characterized by poorly crystalline iron oxides as first reported

[1] Institut d'Astrophysique Spatiale, CNRS/Université Paris-Sud, Orsay, France.
[2] Laboratoire Dynamique Terrestre et Planétaire/UMR5562, Centre National de la Recherche Scientifique, Toulouse, France.
[3] Istituto Nazionale Di Astrofiscia dello Spazio Interplanetario, Rome, Italy.
[4] Geological Sciences, Brown University, Providence, Rhode Island, USA.

0148-0227/07/2006JE002840$09.00

by *Singer and McCord* [1979]. Data from the recent Mars missions show that the mafic regions have much more diversity than previously recognized (see *Christensen et al.* [2005] for a review of the Mars Global Surveyor/Thermal Emission Spectrometer (MGS/TES) and Mars Odyssey/Thermal Emission Imaging System (THEMIS) results, and *Mustard et al.* [2005] for OMEGA). For instance, olivine that can provide clues to the Martian petrology was first identified in a few locations by TES [*Hoefen et al.*, 2003] and THEMIS [*Christensen et al.*, 2003]; then, OMEGA data has confirmed and extended the identification of this mineral to several additional areas [*Mustard et al.*, 2005]. Of special interest are the unambiguous detections of secondary minerals including various phyllosilicates [*Poulet et al.*, 2005], Ca-Mg-Fe sulphates [*Squyres et al.*, 2004; *Arvidson et al.*, 2005; *Gendrin et al.*, 2005; *Langevin et al.*, 2005a] and other Fe^{3+} O-H phases [*Klingelhöfer et al.*, 2004; *Morris et al.*, 2004].

3. Data Set Overview

[5] Following the 25 December 2003 orbit insertion of the Mars Express spacecraft (MEx), the Martian global-scale mapping by OMEGA was initiated. The instrument operates from the visible (0.35 μm) to the thermal infrared (5.1 μm). The present analysis focuses on VNIR reflectance measurements (0.35–2.5 μm). With a fixed IFOV of 1.2 mrad, OMEGA has the flexibility to accommodate modes of operations through cross track swaths of 16, 32, 64, or 128 IFOV in width [*Bibring et al.*, 2004]. Operations of OMEGA are primarily nadir pointed, making surface swath widths ranging from 1.1° to 8.8°. The global maps are primarily derived from observations for which the altitude of the spacecraft ranges from 1500 to 4000 km. In this case, the swath width is 128 pixels, with a pixel size varying from 1.8 to 4.8 km accordingly. The high spatial resolution observations acquired for spacecraft altitudes lower than 450 km and with a swath of 16 pixels width are not considered here, because these tracks are too narrow (~6 km) to contribute to the mapping at a planetary scale.

[6] In this work, maps of the near-infrared (NIR) albedo and global mineralogical distributions are built by using the first 22 months of OMEGA operations, from Ls = 330° to Ls = 315°. This corresponds to 429 orbits and 1468 OMEGA cubes (i.e., ~50 million of spectra) which provide coverage of about 90% of the Martian surface. The OMEGA radiance data are corrected for solar irradiance and atmospheric absorptions in the VNIR using the standard data reduction schemes [*Bibring et al.*, 2005; *Belluci et al.*, 2006], which produces reflectance I/F spectra. I/F corresponds to the ratio of the observed radiance to the incoming solar flux per unit of surface. We have used the OMEGA reflectance data recorded when the operation mode is nadir and the calibration lamp is switched off. The observations that have saturated the detectors are not considered. From orbit number 513, the 128 pixel observation mode produced spurious values for some pixels which were not mapped because a systematic correction of this problem is not yet possible. The northern and southern high-latitude regions are strongly affected by the presence of seasonal icy frosts as well as strong atmospheric variations that precluded systematic mapping [*Langevin et al.*, 2007]. Therefore our mapping was restricted to the latitudes range between −50° and 50°.

4. Identification and Mapping

4.1. Near-Infrared Albedo

[7] A NIR albedo map was produced using the I/F value at λ = 1.08 μm, assuming a lambertian surface. All the spectral parameters listed in Table 1 and described in detail hereafter can be compared to the NIR albedo map.

4.2. Mineral Spectral Parameters

[8] Previous studies show that OMEGA is able to detect unambiguously key surface materials in the form of mafic iron-bearing silicates, hydrated minerals, ferric oxides, and

Table 1. Description of Spectral Parameters Used in This Study[a]

Name	Formulation	Detection Threshold	Rationale
NIR albedo	R(1.08)/cos(i), with i as incidence angle relative to the aereoid	N/A	lambertian albedo
0.55-μm band depth or Fe^{3+} parameter (Figure 1a)	1 − R(0.55)/(0.5*R(0.44) + 0.5*R(0.65))	0	degree of oxidation or amount of dust contamination of the surface
Nanophase ferric oxide or 1/0.8-μm slope (Figure 1b)	R(0.97)/R(0.80)	1	nanophase ferric oxides if ratio > = 1
Pyroxene (Figure 1c)	1 − (R(2.15) + R(2.22))/(R(1.81) + R(2.49))	0.01	2-μm band due to both low-calcium and high-calcium pyroxenes
Forsterite or Mg-rich olivine (Figure 1d)	(0.5*R(1.54) + 0.5*R(1.56))/(0.1*R(1.01) + 0.2*R(1.21) + 0.7*R(1.36))	1.04	1-μm band due to Mg-rich olivine
Fayalite or Fe-rich olivine (Figure 1e)	(0.5*R(1.69) + 0.5*R(1.70))/(0.1*R(1.01) + 0.1*R(1.21) + 0.4*R(1.36) + 0.4*R(1.50))	1.02	1-μm band due to Fe-rich olivine and/or large grain size (>1 mm)
1.9-μm band depth or hydrated mineral (Figure 1f)	1 − (0.5*R(1.93) + 0.5*R(1.94))/(0.5*R(1.83) + 0.5*R(2.12))	0.02	water-bearing minerals
Water ice	1 − (R(1.50) + R(1.51))/(R(1.30) + R(1.71))	0	1.5-μm band due to water ice
CO_2 ice	1 − R(1.43)/(0.5*R(1.38) + 0.5*R(1.44))	0	1.43-μm band due to CO_2 ice

[a]R is the reflectance I/F at a given wavelength λ (μm).

ices [*Bibring et al.*, 2005, 2006]. VNIR spectral properties can be categorized in terms of a set of spectral parameters. The spectral parameters (also called spectral index or spectral criterion hereafter) considered in this study are listed in Table 1. They were developed for a few minerals representative of the Martian mineralogy, and applied to analyze the I/F atmospheric-corrected spectra. The pyroxene index uses the 2-μm band attributed to crystal field transitions in Fe^{2+} which preferentially occupy the M2 crystallographic site [*Gaffey et al.*, 1993]; this spectral index is sensitive to both low- to high-calcium species. Two olivine indexes (Mg-rich olivine and Fe-rich olivine) are based on the strong and broad 1-μm band of olivine mineral due to Fe^{2+} ion in distorted octahedral sites [*Gaffey et al.*, 1993]. The 1.9-μm band attributed to overtone of the H-O-H bending mode and the OH stretching mode was used to identify water-bearing minerals or hydrated minerals [*Gaffey et al.*, 1993]. The content of Fe-oxidized phases is measured thanks to an Fe^{3+} parameter based on the combination of spectral features in the visible due to the presence of Fe^{3+} ions [*Morris et al.*, 1989]. The presence of nanophase ferric oxide is based on the spectral shape of absorptions in the 0.8–1-μm wavelength region resulting from the grain size effect [*Morris et al.*, 1989].

[9] The data analysis based on spectral parameter has the advantage of being fast and well adapted for the large OMEGA data set. However, mineral abundances are not reported here because the strength of each spectral index depends on a variety of parameters such as the mineral mixture, the relative concentration, the optical constants and the grain size distribution of each end-member, the surface texture and the atmospheric condition. Mineral deconvolution using complex radiative transfer theory is needed to provide concentrations [*Poulet and Erard*, 2004]. Since such a method is very time consuming, it has not yet been applied to the entire OMEGA data set. However, limits of detection in term of abundance are discussed for the olivine and hydrated minerals (section 4.3.4).

[10] Finally, we note that some important minerals such as feldspar, quartz, amorphous silica, and nonhydrated salts are not mapped here because they are featureless in the OMEGA wavelength range. VNIR data are actually well suited for Fe and hydrated minerals, whereas thermal infrared (TIR) measurements are well suited for a broad range of silicate and other minerals that do not show visible–near infrared absorptions (e.g., feldspar). Both wavelength regions are differentially affected by texture, coatings, and particle size. For example mineral identification in the TIR, can be hampered by fine particulate textures.

4.2.1. Ferric Phases

[11] Telescopic, orbital, and in situ observations have revealed the presence of ferric iron absorption features in the UV/visible that are indicative of oxidized surface materials. The strength of the ferric absorption edge at 0.53 μm provides a good estimate of the degree of oxidation or amount of dust contamination of the surface [*Bell et al.*, 1993; *Morris et al.*, 2000; *Farrand et al.*, 2006]. This absorption edge is caused by several effects: intense Fe^{3+} ligand field transitions between 0.4 and 0.6 μm, Fe^{3+} electronic pair transitions in the 0.5–0.7-μm region and a strong $O^{2-} \rightarrow Fe^{3+}$ charge transfer absorption centered near 0.25–0.35 μm. To study this feature, we use the spectral parameter that is defined by *Morris et al.* [2000] and called BD530 in their paper, and addresses the depth of the 0.53-μm absorption feature. The positions of the BD530 wavelengths have been slightly adapted to account for the OMEGA spectral resolution (Table 1 and Figure 1a). This Fe^{3+} parameter can be positive or negative depending on the deviation from the reference line. As shown by *Morris et al.* [2000], the values of the Fe^{3+} spectral parameter increase in the following order: jarosite (negative values) < maghemite (positive values) < nanophase oxides < hematite.

[12] Ferric phases also exhibit a broad NIR absorption feature between 0.75 and 1.0 μm resulting from electronic transitions and which in some instances are indicative of the degree of crystallinity and iron content. More specifically, the spectral ratio of the reflectance at wavelengths 0.97 and 0.8 μm is a good index of the nature of ferric oxide and provides a second parameter for ferric phases and called the 1/0.8-μm slope (Table 1 and Figure 1b) [*Bell et al.*, 2000]. As a test, the 1/0.8-μm slope parameter has been calculated for the laboratory samples of hematite particles smaller than 10 nm (samples S6FN-type D from *Morris et al.*, 1989]) and typical values ranged between 1.0 and 1.05 were obtained. Values close to or slightly larger than 1 can be thus assigned to the presence of nanophase ferric oxides. Small deviations from linearity and second-order effects can result in instrumental errors on the order of a few percent when comparing reflectance spectra in this wavelength range [*Belluci et al.*, 2006]. Given these uncertainties, the values larger than unity is considered as a diagnostic of the presence of so-called nanophase ferric oxide, with size of a few tens of nm or less [*Morris et al.*, 1989, 1993].

4.2.2. Pyroxene

[13] Mafic minerals play an important role in determining the history of the Martian geology. The detection of pyroxene is made on the basis of the presence of a broad 2-μm absorption corresponding to a mixture of low-calcium pyroxene (LCP), for which the band is centered at $\sim$1.9 μm, and high-calcium pyroxene (HCP), for which the band is centered at $\sim$2.3 μm. The pyroxene spectral parameter is defined in Table 1, and an example of a typical pyroxene-rich spectrum is illustrated in Figure 1c. To account for instrumental and atmospheric biases, the detection is considered positive for values of the pyroxene spectral parameter larger than 1%. Our spectral parameter is not designed to discriminate between the LCP end-member and HCP end-member. It has been demonstrated that other methods such as the Modified Gaussian Model (MGM) are very efficient to achieve this goal [*Bibring et al.*, 2005].

4.2.3. Olivine

[14] Olivine has a broad, complex absorption centered near 1 μm that varies in width, position, and shape with grain size and Fo number. For instance, the right wing shifts toward longer wavelengths as the amount of FeO in the olivine increases. In USGS samples [*Clark et al.*, 1993], the absorption feature extends to $\sim$1.55 μm for Fo89 and to $\sim$1.8 μm for Fo11. The increase in grain size broadens the bottom of the band and shifts the right wing of the band toward longer wavelengths, so that a forsterite olivine spectrum with very large grains ($\gg$100 μm) and a fayalite olivine spectrum with smaller grain have similar spectral features. Nevertheless, we have defined a spectral index for

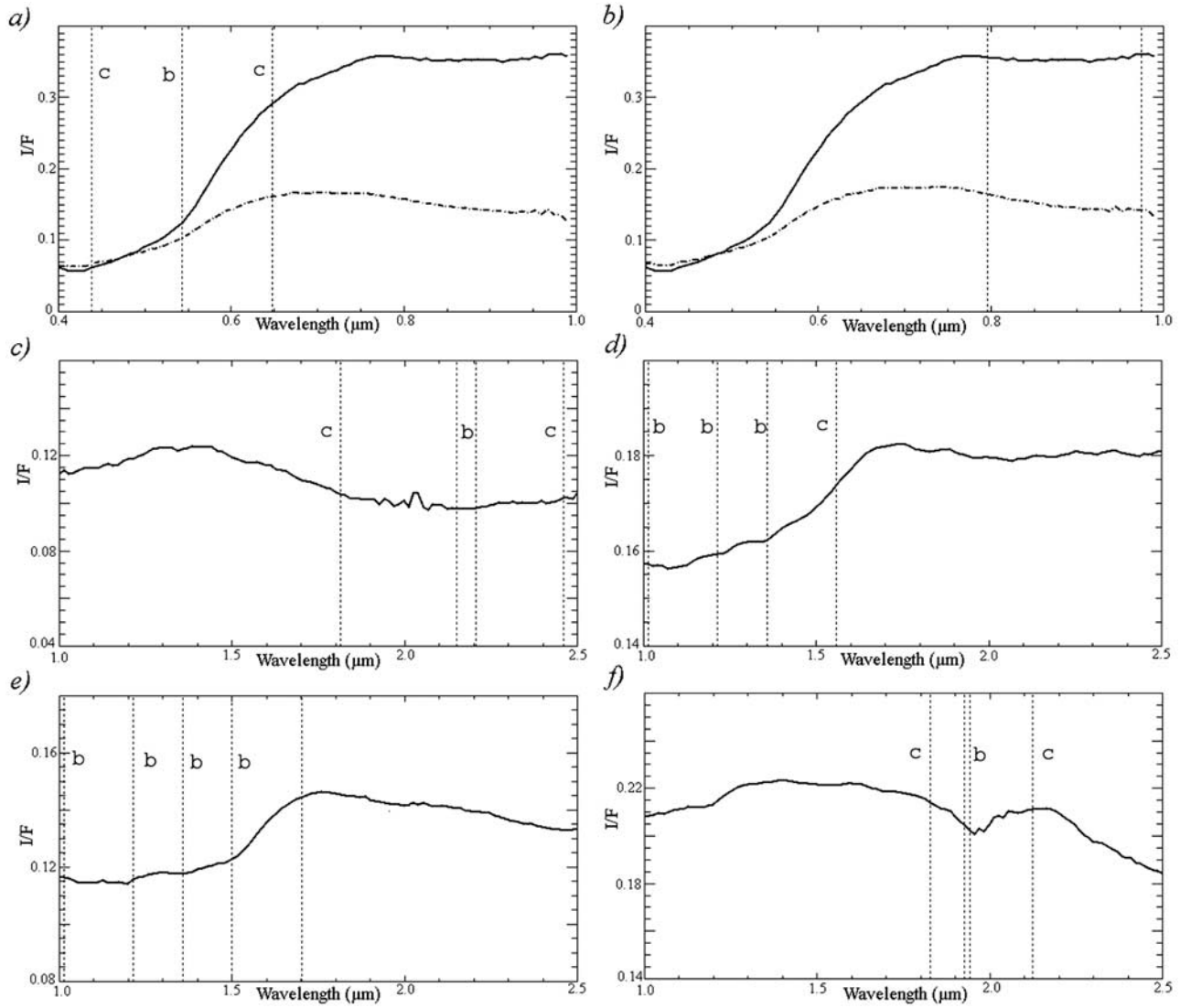

Figure 1. Band positions of spectral parameters listed in Table 1 on OMEGA spectra representative of the major spectral types discussed in the paper. (a) Fe^{3+} parameter over typical spectra of dark (dashed line) and bright regions (solid line), (b) nanophase ferric oxide parameter over typical spectra of dark (dashed line) and bright regions (solid line), (c) pyroxene parameter over a typical spectrum of a pyroxene-rich terrain, (d) forsterite parameter over a spectrum of a olivine-rich (likely enriched in Mg) deposit, (e) fayalite parameter over a spectrum of a olivine-rich (likely enriched in Fe) deposit, and (f) 1.9-μm parameter over a spectrum of water-bearing terrains identified by the 1.9-μm band. The vertical dashed bars indicate the wavelengths used for the band centers (labeled by b) and the wavelengths used for the continuum (labeled by c) used in the calculation of the spectral parameters (Table 1).

each of the two olivine end-members (forsterite and fayalite) based on the spectral slope in the 1.0–1.7-μm region. The formulas of these two olivine parameters are given in Table 1 and the spectra representative of these minerals are shown in Figures 1d and 1e. In typical olivine-free Martian spectra, the indexes are less than unity; presence of olivine increases these indexes above unity. For instance, we observe values larger than 1.1 for the forsterite and fayalite parameters in the Nili Fossae region where the identification of olivine is certain. However, an index slightly higher than unity can also reflect the presence of crystalline ferric oxides or of pyroxene and/or be due to atmospheric effects. Therefore, in order to remove ''false positive'', we have set a threshold for olivine detection to 1.04 for the forsterite index, and to 1.02 for fayalite, after proper evaluation based on careful analysis of OMEGA data set and on spectra of terrestrial samples. For instance, the forsterite parameter calculated for the spectrum of the terrestrial fine-grained (<45 μm) forsterite (sample LAP050 of the MRO/CRISM library [*Bishop et al.*, 1995]) is equal to 1.15, while the value of the fayalite parameter of the spectrum of the terrestrial fine-grained (<45 μm) fayalite (sample LAP005 [*Bishop et al.*, 1995]) is 1.70.

[15] We excluded spots identified by a forsterite index larger than 1.04 for which the spectrum exhibits a strong raise between 1.0 and 1.4 μm, combined with a shallow

1.0-μm feature (nanophase ferric oxide index larger than 0.94). These spectral properties are typical of poorly crystalline ferric oxides with grain sizes ranged between several hundreds of nanometers and several tens of micrometers [*Morris et al.*, 1989]. Such spots are found in a few areas only: Terra Meridiani, Valles Marineris, and Aram Chaos.

[16] Finally, comparison of our technique mapping with MGM deconvolution results produced over Syrtis Major [*Pinet et al.*, 2006] suggests that for the forsterite index, olivine might be present in association with pyroxene for a threshold as low as 1.025–1.03. Accordingly, as a critical assessment of sensitivity on the extent of the olivine distribution map at the global scale, this second threshold could be considered as a proxy for marginal.

4.2.4. Hydrated Minerals

[17] OMEGA detects hydrated minerals by the presence of an absorption feature resulting from overtones and combinations of OH and H_2O in the 1.9-μm wavelength region. This absorption feature is measured at $\sim$1.93 μm with a continuum at 1.83 μm (1.80 μm for the orbit number larger than 2100 because of an instrumental problem that affects the 1.83-μm spectral element) and 2.12 μm, as illustrated in Figure 1f. This absorption feature serves as an indicator of hydrated minerals; it has been used in previous studies for mapping minerals considered to result from aqueous alteration processes and include phyllosilicates [*Poulet et al.*, 2005; *Loizeau et al.*, 2007; *Mangold et al.*, 2007] and sulfates [*Langevin et al.*, 2005a]. A threshold of 0.02 is used in order to be significantly above instrumental noise and atmospheric artifacts. Some sulfates (kieserite and romerite), are excluded in this mapping because the 1.9-μm hydration band of these minerals is shifted to longer wavelengths [*Gendrin et al.*, 2005; *Cloutis et al.*, 2006].

4.3. Uncertainties

4.3.1. Uncertainties Due to Ices

[18] OMEGA is very sensitive to the presence of ice, under the form of clouds and frosts [*Bibring et al.*, 2005; *Gondet et al.*, 2006]. Both water ice and carbon dioxide ice have an absorption band centered at $\sim$2 μm, which may affect the detection of hydrated minerals. In mapping the hydrated minerals, we therefore decided to disregard spectra in which either H_2O ice, identified by its 1.5-μm absorption band, or CO_2 ice, identified by its 1.43-μm absorption band [*Langevin et al.*, 2005b; *Langevin et al.*, 2007] are detected. The ice criteria are described in Table 1.

[19] Pyroxene and olivine detection mapping can be also biased by the presence of ices. Therefore we do not plot pixels with H_2O ice criterion larger than 0.2, 0, and 0.1 when mapping pyroxene, forsterite and fayalite respectively, and with CO_2 ice criterion larger than 0 for all three maps.

4.3.2. Uncertainties Due to Aerosols

[20] To discriminate spectral features related to fine-grained surface coatings from those originating from the atmospheric dust is a difficult task, because a dusty atmosphere may have spectral signatures similar to those of the surficial dust. The strongest contribution of aerosols in term of spectral signatures and quantitative effects is expected to occur in the visible wavelength range. Since atmospheric conditions are variable, the values of the spectral parameters would vary with time if the detection was dominated by suspended dust. OMEGA was able to target some geographic regions on Mars several times, at different local times and/or seasons, providing the opportunity to check the temporal variation of the spectral parameters. As expected, the visible portion of the electromagnetic spectrum is the most affected and shows significant absolute variations related to the magnitude of the Fe^{3+} parameter. However, the relative differences of the parameter from one region to another one do not change both at the regional and global scales, and the effects of the variable atmospheric conditions are negligible on the global maps.

4.3.3. Uncertainties Due to Fine Grain Coatings

[21] Laboratory and field investigations of the spectral effects of fine surface grain coating have shown that thin (<100 μm) layers can partly or totally mask the underlying materials in both the visible and near-infrared portions at the spectrum [*Singer and Roush*, 1983; *Wells et al.*, 1984; *Fischer and Pieters*, 1993; *Christensen et al.*, 1998]. However, this masking effect is known to be less important in the NIR wavelength region than in the visible wavelength interval, because of the increasing transparency of the surface coating at longer wavelengths. Thus the NIR absorption bands of pyroxenes and hydrated minerals can be detected despite the presence of an optically thick coating. A dust coating over dark substrate results in a negative slope of the spectrum in the near-infrared because of increasing transparency of the coating at longer wavelengths, resulting in a greater contribution from the substrate [*Singer and Roush*, 1983], and/or by a dependence of the phase function with wavelength [*Johnson and Grundy*, 2001]. Since the dark surfaces on Mars likely are basaltic in composition, such observation can be considered as an indirect detection of a basalt material as discussed in sections 5.4 and 6.3.

[22] Finally, previous works using mapping technique based on spectral parameters [*Langevin et al.*, 2005a; *Poulet et al.*, 2005; *Mustard et al.*, 2005] have shown that most of the regions exhibiting spectral signatures of mafic or water-bearing materials are very well correlated to distinct and specific geological units. This gives us strong confidence in the technique consisting of mapping the minerals with spectral parameters.

4.3.4. Uncertainties Due to Grain Size and Mixture

[23] The grain size distribution of a mineral mixture affects the absorption band depth and thus detection limits of the material in the mixture. Optimal particle size for each absorption feature for specific mineral of a given texture that maximizes its band depth has been observed by many workers [e.g., *Clark and Lucey*, 1984; *Hapke*, 1993]. For mafic material, the optimal particle size is ranged between a few tens of and a few hundred micrometers [*Harloff and Arnold*, 2001]. Accurate determination of the grain size distribution is critical for olivine, because its 1-μm absorption band depth is strongly affected by the grain size. To test the robustness of the forsterite spectral parameter and of the threshold of detection, we performed tests on two series of synthetic spectra that we have created using a radiative transfer model [*Poulet and Erard*, 2004]. Figure 2 shows synthetic spectra of intimate mixtures of Mg-rich olivine grain (100 μm in size), diopside grain (200 μm), pigeonite grain (50 μm) and labradorite grain (100 μm). The effect of the different concentrations of olivine (from 0% to 30% by step of 5%) can be seen on the spectra. Increasing the

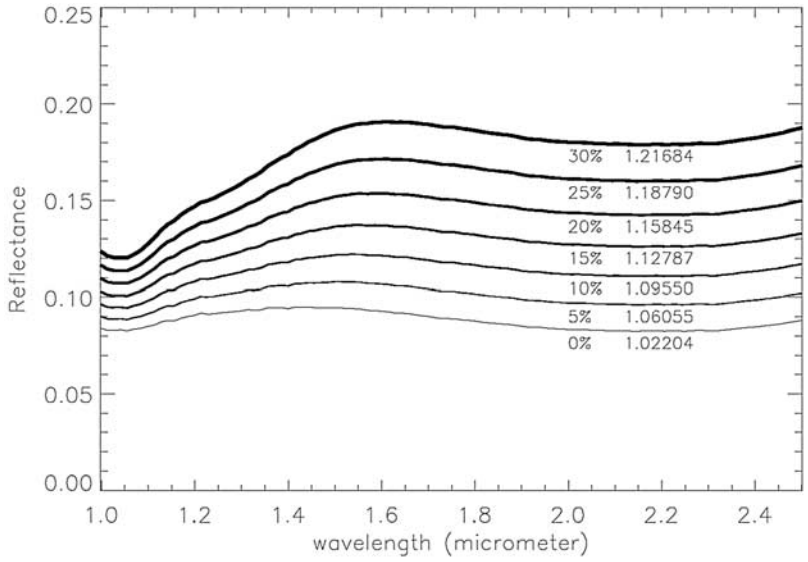

Figure 2. Synthetic spectra of intimate mixtures of high-calcium pyroxene, low-calcium pyroxene, and plagioclase mixed with varying concentrations (0%, thinnest line, to 30%, thickest line) of Mg-rich olivine of 100-μm grain in size. All the parameters are fixed except for the concentrations of the olivine and plagioclase (plagioclase concentration decreases when olivine concentration increases). The calculated value of the forsterite spectral parameter is indicated for each spectrum. We assume that the detection is considered positive for the OMEGA data set if the spectral parameter is larger than 1.04 (see text).

olivine abundance increases the 1-μm band signature and the value of the forsterite spectral parameter. It appears that a mixture with an olivine concentration of 5% only gives a fairly straightforward detection (forsterite spectral parameter equal to 1.06). Figure 3 shows the result for a same set of parameters except for the olivine grain size, set here at 10 μm. In this case, the detection is negative below a concentration of 20%, and even at this concentration, the spectrum does not exhibit a significant absorption of olivine. This second simulation represents a "worst case" for the olivine detection; increasing the grain size and/or decreasing the Fo number strongly favors the identification of the olivine by OMEGA. An important outcome of these results is that we may not accurately identify olivine in mixtures such as the pyroxene-rich regions that could contain as much as 20% forsterite, if the olivine grain size is in the micrometer range.

[24] The effects of fine particle size distribution on reflectance spectra of hydrated minerals have been investigated in laboratory measurements using a montmorillonite clay [*Cooper and Mustard*, 1999]. While significant decreases in band depths at 1.4, 1.9, and 2.2 μm are observed as particle size decreases, the band strength of

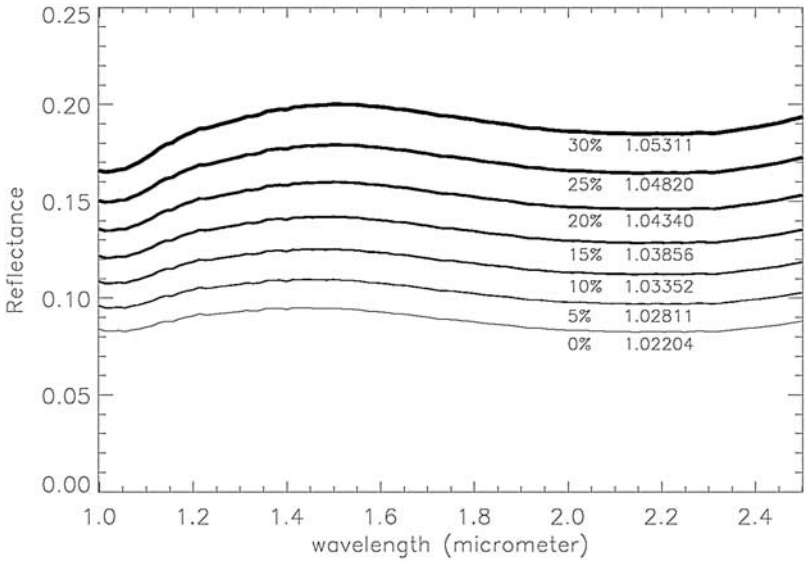

Figure 3. Same as in Figure 2 except that the grain size of the olivine component is 10 μm.

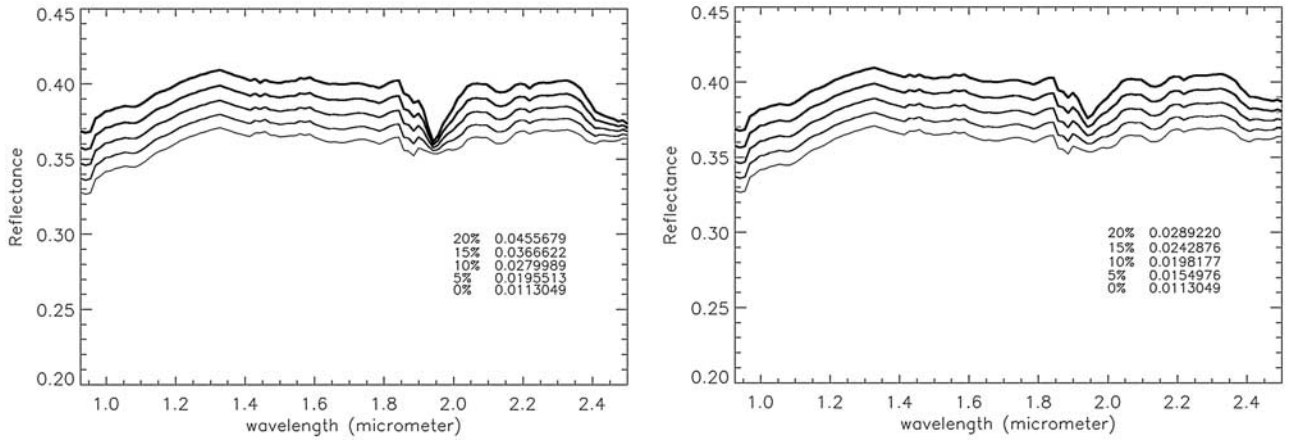

Figure 4. Synthetic spectra of intimate mixtures of gypsum and Martian-like dust for two grain sizes of gypsum: (left)10 μm and (right) 5 μm. All the parameters are fixed except for the concentrations of the gypsum and the dust (from 0%, thinnest line, to 20%, thickest line). The dust concentration decreases when the gypsum concentration increases. The value of the 1.9-μm spectral parameter is indicated for each spectrum and its corresponding abundance. We assume that the detection is considered positive if the parameter is larger than 2%.

the 1.9-μm feature for sample of size <5 μm is several percent, i.e., still significantly larger than the identification threshold of 2% used in our study. However, when hydrated minerals are mixed with other constituents, the 1.9-μm band depth could be reduced, decreasing the lower limit of detection of hydrated minerals in the Martian soil. Using the depth of the 1.9-μm absorption band in synthetic mineral mixtures containing a hydrated mineral (gypsum) and Martian dust, we were able to develop a similar understanding. The gypsum mineral has been chosen for this experiment since their optical constants are now available [*Roush et al.*, 2006]. As the optical constants of the Martian dust are not known, we used empirical methods described by *Shkuratov et al.* [1999] to numerically estimate the imaginary index of the constituent using normal reflectance spectrum of the northern bright regions. The effect of the different abundances of gypsum (from 0% to 20% by step of 5%) mixed with Martian-like dust can be seen on the spectra (Figure 4). The greater the abundance of the gypsum, the deeper the band, the higher the value of the 1.9-μm spectral index. We note that a mixture with a gypsum concentration slightly greater than 5% (10%) can be considered as a positive detection assuming a gypsum grain size of 10 μm (5 μm).

[25] Finally, the regions that unambiguously exhibit a 1.9-μm band correspond to well-defined geological units [*Gendrin et al.*, 2005; *Langevin et al.*, 2005a; *Poulet et al.*, 2005; *Mangold et al.*, 2007; *Loizeau et al.*, 2007]. Although we may not detect all the hydrated material using this technique, a good correlation exists between the mineralogical units and the geomorphologic units, which reinforces our confidence in detection mapping technique.

5. Results

[26] In this section we present the global maps for each component and using the spectral index discussed above. All maps have a resolution of 32 pixels per degree (~2 km at the equator).

5.1. NIR Albedo

[27] Figure 5a shows the NIR albedo map. The major trends are the same than those of the visible albedo map or bolometric albedo [*Mellon et al.*, 2000; *Ruff and Christensen*, 2002]. The bright regions (NIR albedo greater than 0.3, one typical example is shown in Figure 1a) are localized in the northern hemisphere with the highest albedo found over the Tharsis region. The low NIR albedo regions (less than 0.2) are mainly localized in Syrtis Major and in the southern highlands, although low NIR albedo regions such as Acidalia are also identified in the northern hemisphere. The highest NIR albedo is near 0.45 which is about 10% larger than the values found on Pathfinder at 1.0 μm [*Bell et al.*, 2000]. These values are significantly greater than the highest reflectance of 0.38 derived from past terrestrial observations [*Bell*, 1992; *Murchie et al.*, 2000], but in general agreement with the albedo map derived from observations at 0.98 μm made by *De Grenier and Pinet* [1995]. The discrepancies with some previous observations could result from physical processes (temporal variations of the contribution of the aerosols, photometric effects due to the different geometries of observations). Calibration issues cannot be totally excluded, but the observed differences are inside the errors of the absolute calibration of OMEGA (<20% from *Bonello et al.* [2005]). The lowest values (~0.09 over Syrtis Major) are close to the lowest-albedo units found by Pathfinder [*Bell et al.*, 2000] and past observations [*De Grenier and Pinet*, 1995; *Murchie et al.*, 2000].

[28] It should be noted that the map has been produced from observations taken at various seasonal times, day times and spatial resolutions. Nevertheless, regions of uniform albedo do not show significant variations between overlapping orbits. This supports the idea that neither the scattering properties of the surface nor the atmospheric conditions significantly affect the NIR part of the spectrum, and that the lambertian approximation for the surface is a legitimate approximation.

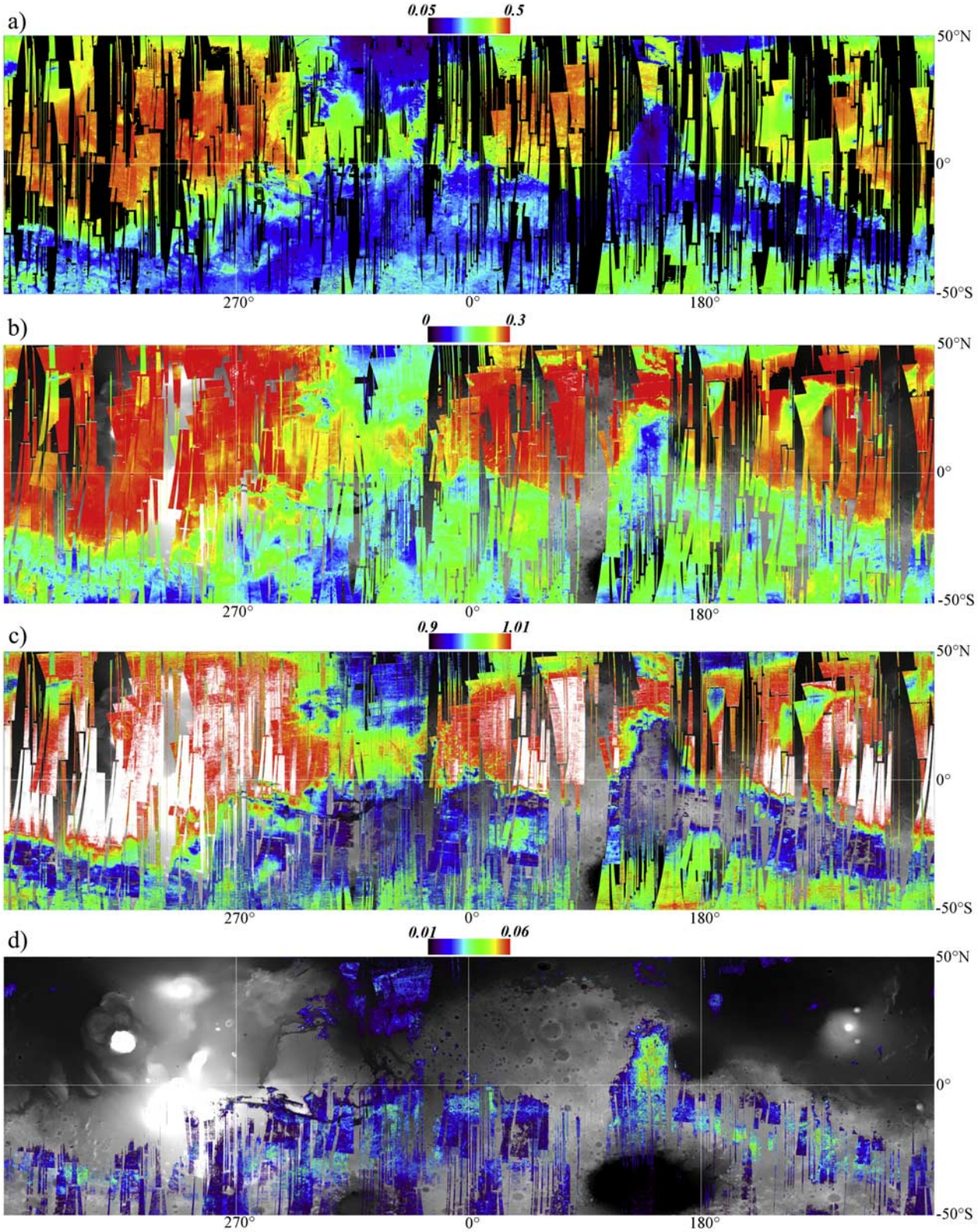

Figure 5. The 32 pixel per degree binned global spectral parameter maps over MOLA map: (a) NIR albedo, (b) Fe^{3+} phase, (c) nanophase ferric oxide, and (d) pyroxene. The scales are indicated for each map. Pixels with values below the detection limit are not plotted. Colors that are above the scale are in white.

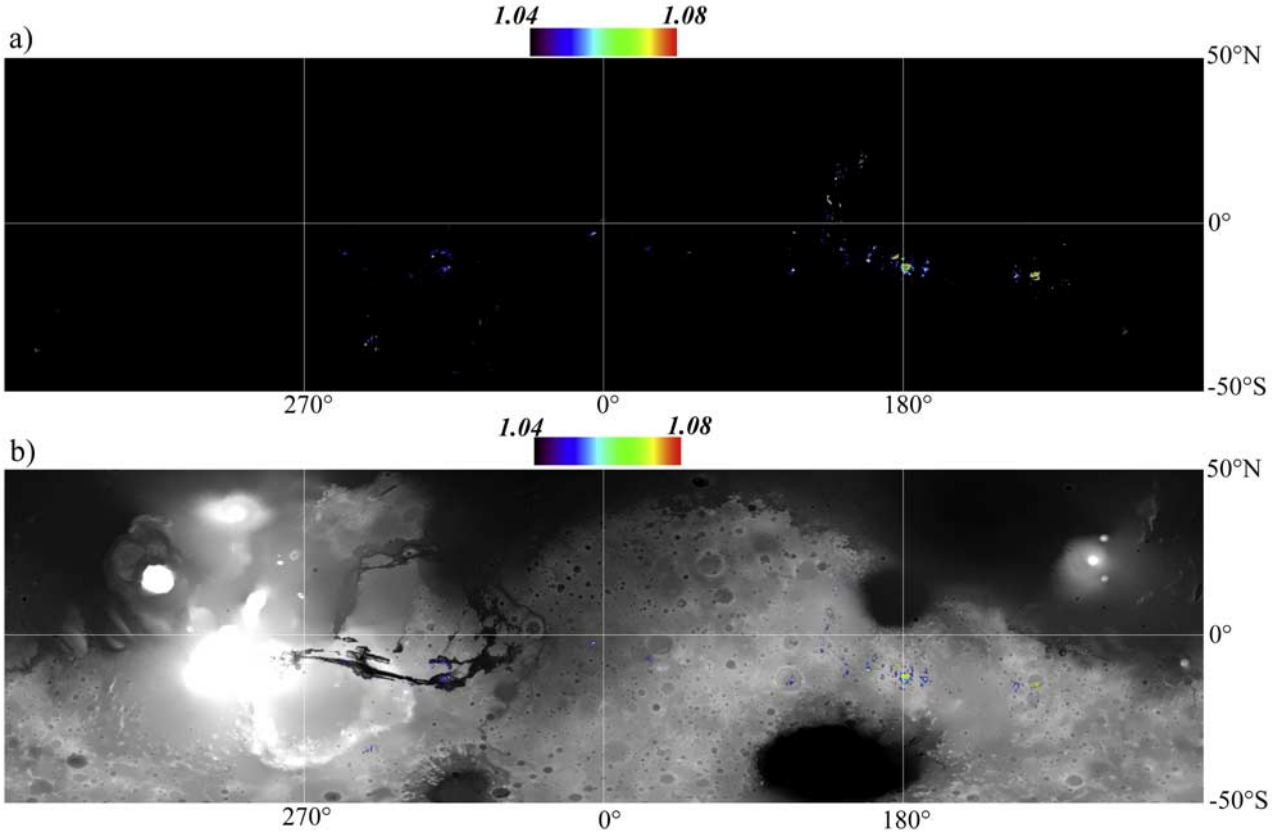

Figure 6. (a) Global distribution of forsterite parameter on a black background and (b) the MOLA altimetry. Colors that are above the scale are in white.

5.2. Fe^{3+} Feature

[29] As shown in Figure 5b, values of the Fe^{3+} spectral parameter are positive for all the OMEGA pixels. This implies the presence of ferric oxide phases everywhere at the surface, although its abundance varies significantly. These variations reflect the existence of distinct mineral phases, with different composition and origin, in the various units. Although atmospheric effects may be present, the map shows a remarkable spatial coupling of the value of the Fe^{3+} spectral index and the NIR albedo. The greatest values found in the bright regions are close to 0.3, which is larger than the values found for the brightest Pathfinder soils. On terrestrial analogues, similar large values were derived for nanophase ferric oxide [*Morris et al.*, 2000].

5.3. Nanophase Ferric Oxides

[30] The global map of the nanophase ferric oxides (hereafter abbreviated np-Ox) obtained from the 1/0.8-μm slope parameter mapping is presented in Figure 5c. The darkest regions have values of the 1/0.8-μm slope parameter smaller than 0.9 because of strong mafic 1-μm bands and are not plotted on the map. The white regions represent values greater than 1.01 and their spectra are thus characterized by significant red slopes (increasing reflectance with increasing wavelength) between 0.8 and 1.0 μm. No obvious artifacts due to atmospheric effects are evident. Apparent from the map is the spatial coherence of the largest values (red and white areas on Figure 5c) with the bright regions in the NIR albedo map (Figure 5a). Consequently, the values of the Fe^{3+} and nanophase ferric oxide parameters of the bright regions are consistent with previous telescopic and spacecraft investigations that have implied np-Ox as the best spectral analogues to these regions in the VNIR wavelength range. Nevertheless, some spectra of these regions (Figure 1b) exhibit a very weak 0.9-μm range inflection, which could be explained by the presence of a minor amount of poorly crystalline ferric phase.

5.4. Pyroxene

[31] Pyroxenes are identified in equatorial and southern low-albedo regions with the highest parameter values found in Syrtis Major (Figure 5d). This map is consistent with the TES global pyroxene map [*Bandfield*, 2002] and with the map derived from OMEGA observations analyzed with the Modified Gaussian Model [*Bibring et al.*, 2006]. Identification of the pyroxene in the low-albedo regions of the northern hemisphere is positive while challenging because the value of the pyroxene spectral parameter is close to the detection threshold equal to 0.01. These regions are spectrally rather unique and are best characterized by a blue slope in the NIR range (decreasing reflectance with increasing wavelength) [*Mustard et al.*, 2005, Figure 5]. They exhibit a weak 2-μm band but no apparent 1-μm band.

5.5. Olivine

[32] Olivine is mapped according to its two spectral parameters: forsterite and fayalite (Table 1 and Figures 1d, 1e, 6, and 7). Thresholds and potential biases are discussed

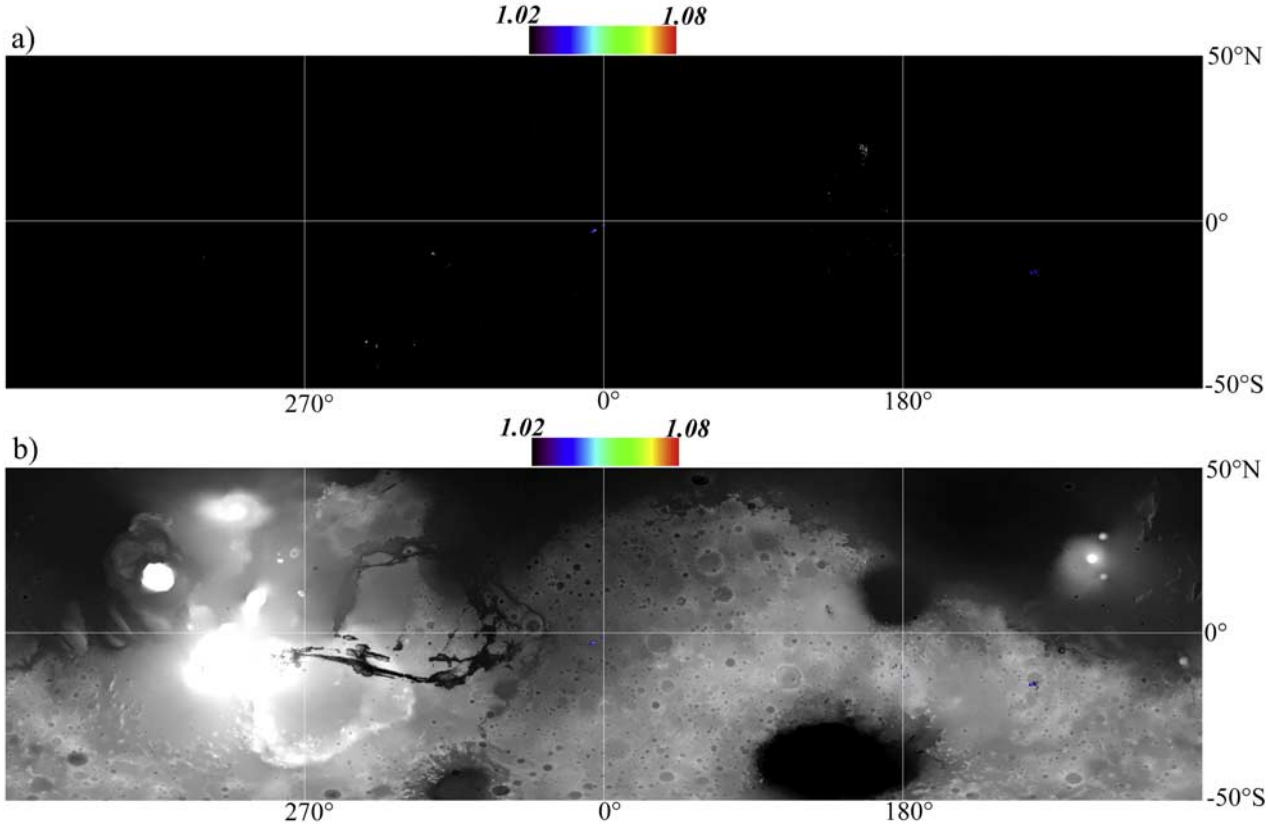

Figure 7. Same as in Figure 6 but for the fayalite parameter.

in sections 4.2.3 and 4.3.4. These maps provide the first global olivine distribution map of Mars based on OMEGA observations.

5.5.1. Mg-Rich Olivine

[33] All previously identified olivine regions are detected using the forsterite spectral parameter and include Nili Fossae, Terra Meridiani, Syrtis Major and Ganges Chasma [*Bandfield*, 2002; *Christensen et al.*, 2003; *Hoefen et al.*, 2003; *Hamilton and Christensen*, 2005; *Mustard et al.*, 2005]. Regions of large areal concentration of Mg-rich olivine have been also identified in the low-albedo regions: Aonia terra, Nereidum Montes, western rim of Isidis basin, Terra Tyrrhena, Oenotria Scopulus as well as in several unnamed and named craters (Gale, Herschel, Huyghens, Schroeter, Pollack), southwest of Schiaparelli crater, west of Herschel crater, in Valles Marineris (Ius, Hebes, Capri, and Melas). Several isolated concentrations of olivine around the rims of Argyre and Hellas have been identified but are not obvious on the global map because of their small size. Figure 8 shows the Argyre region and a large number of small olivine-rich spots.

[34] A comparison of the pyroxene map (Figure 5d) and the forsterite map (Figure 6) shows that many large areas of olivine are spatially correlated to pyroxene-rich regions, as proposed by *Pinet and Chevrel* [1990]. These observations are also quite consistent with previous works by *Christensen et al.* [2000], who model 12% olivine for basaltic surface composition (TES type I), and *McSween et al.* [2006], who describe detectable amounts of olivine in the low-albedo regions. When we map the forsterite spectral parameter in removing all pixels showing positive detections of pyroxene, we obtain a distribution very similar to the fayalite map (section 5.5.2). This confirms that most of the olivine identified on Mars occurs with pyroxene. Figure 9 illustrates the spectral characteristics of such a typical pyroxene/olivine mixture. Both the shape and band depth of the olivine feature that is observed in the spectral ratio indicate Mg-rich olivine.

[35] Finally, it is important to note that most of the pyroxene-rich terrains show an olivine index below the detection

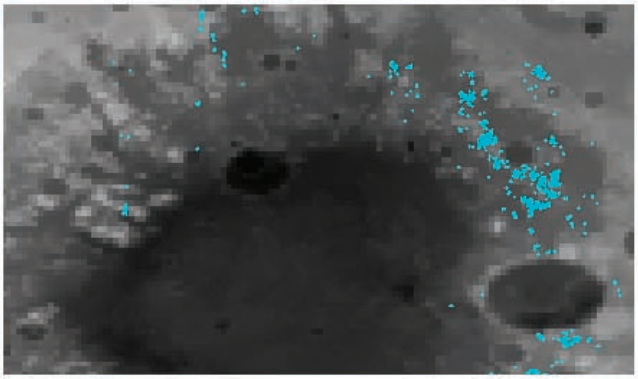

Figure 8. Map of Argyre showing locations of small deposits of olivine using the forsterite criterion. To make them visible on the map, the size of the blue squares is about 5–20 times larger the real size of deposits depending on the spatial resolution of OMEGA swaths.

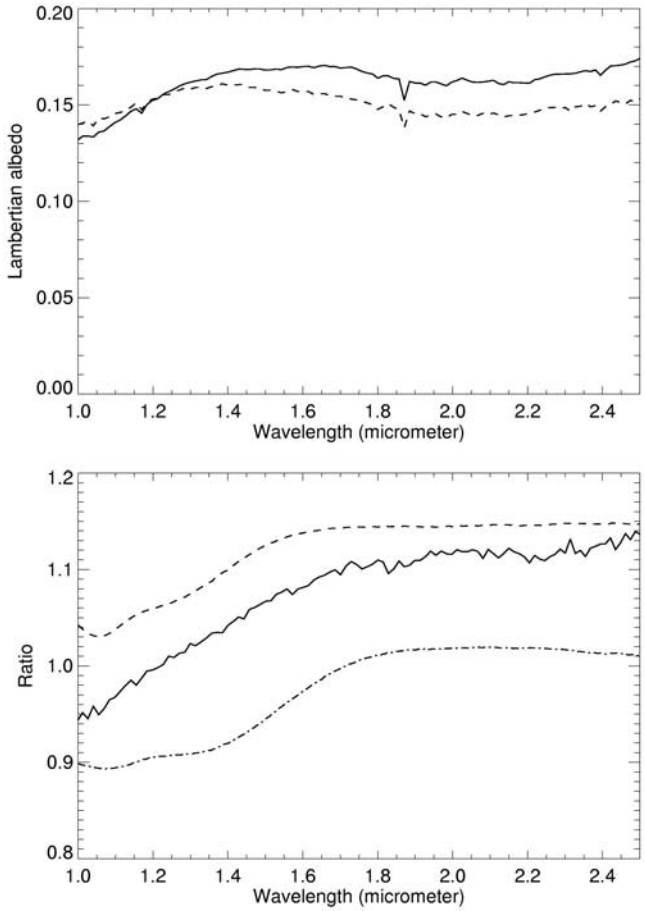

Figure 9. Identification of olivine mixed with pyroxene. (top) The spectrum (continuous line) of a terrain located at 90.9°E, 12.5°S exhibiting both an olivine band (forsterite criterion = 1.045) and a pyroxene band is compared to a pure pyroxene terrain (dashed line). (bottom) Ratio of the two spectra enhancing the 1-μm olivine band compared to laboratory spectra of fayalite (dash-dotted line) and forsterite (dashed line) of grain size smaller than 45 μm.

threshold (Figure 6). As discussed in section 4.3.4, we may not accurately identify olivine in mixtures. Given our mapping technique, the detection threshold and the uncertainties in the data, we cannot exclude that the low-albedo regions may contain small amount (20% at most) of Mg-olivine with small grain size (10 μm or less) mixed with pyroxene and others minerals.

5.5.2. Fe-Rich Olivine

[36] The map of the fayalite spectral index (and/or large grain size of forsterite) shows that this mineral is remarkably limited both in occurrence and in areal coverage at the surface. These olivine-rich terrains correspond to the deposits discussed by *Mustard et al.* [2005].

5.6. Hydrated Minerals

[37] Figure 10 shows the global distribution of the 1.9-μm absorption band on Mars. Hydrated minerals are only detected in four areas at a global scale: Terra Meridiani, Mawrth Vallis, Nili Fossae and Aram chaos. Sulfate-rich terrains in Valles Marineris are difficult to identify at this scale because they are enriched in kieserite which has an absorption band at 2.1 μm (instead of 1.9 μm) and they occur in small isolated areas. Apart from these regions, the surface of Mars from 50°S to 50°N, including the bright northern regions, is remarkably lacking in hydrated minerals at the detection threshold limit discussed in section 4.3.4.

6. Discussion

6.1. Ferric Phases

[38] Because increasing values of the Fe^{3+} parameter are measures of increasing depth of the ferric absorption edge, the variation of this spectral parameter can be interpreted as tracing the degree of alteration in terms of oxidation state. The dark terrains that exhibit the lowest values of the parameter would be the least altered ones, with the presence of the oxidized phases produced by further oxidation or further deposition. Alternatively, their ferric content could come from pristine ferric-bearing minerals. The brightest terrains would be surface covered by the most altered minerals, with respect to the Fe oxidation state. There is no clear dependence with elevation, although the lowest values of the Fe^{3+} criterion are found in the southern highlands. The low-altitude basins Argyre, Hellas, and Isidis do not show a strong enhancement of the Fe^{3+} criterion, while both high- and low-altitude terrains in the Tharsis region and in the northern plains have the largest values of the Fe^{3+} parameter. These values ($\sim$0.3, i.e., 30% band depth) and the spectra from these regions are similar to those obtained with terrestrial nanophase oxides [*Morris et al.*, 2000]. These observations thus suggest that a large fraction of the Martian surface is spectrally dominated by a single component, np-Ox, which is in good agreement with previous works [*Bell*, 1992; *Morris et al.*, 1997]. This composition is actually reinforced by the in situ Mössbauer observations on Spirit that demonstrated that the dust at Gusev crater was dominated by np-Ox [*Morris et al*., 2006].

[39] An important outcome of the OMEGA results has to do with the hydrous state of these nanophase ferric oxides based on the 1.9-μm absorption band, which could not be assessed before. Indeed, the UV/visible spectral characteristics of the ferric phases cannot discriminate between hydrous or anhydrous ferric oxides. In the TIR regime, recent works by *Ruff and Christensen* [2002] using TES data conclude that the bright Martian surface is dominated by plagioclase feldspar particles << 100 μm in size that could have a significant zeolite component [*Ruff*, 2004]. The analysis in the 1–2.5-μm wavelength range provided by the OMEGA data set shows that the 1.9-μm band depth of these bright regions is below the 2% detection limit, supporting the presence of anhydrous np-Ox [*Bibring et al.*, 2006]. It has been proposed that these np-Ox results from a weathering process that does not require liquid water involved [*Bibring et al.*, 2006]. This weathering product could be either in situ processed bedrock and/or mobile ("dust").

[40] In Figure 5c, three large areas enriched in np-Ox appear: Tharsis, Arabia, and Elysium. Thermal inertia values in these regions are typically lower than about 120 [*Mellon et al.*, 2000]. This suggests that these regions are composed of deposits of fine-grained material (6 μm or less [*Presley and Christensen*, 1997]) reaching a depth of a few centimeters thick at least [*Mellon et al.*, 2000]. A strong

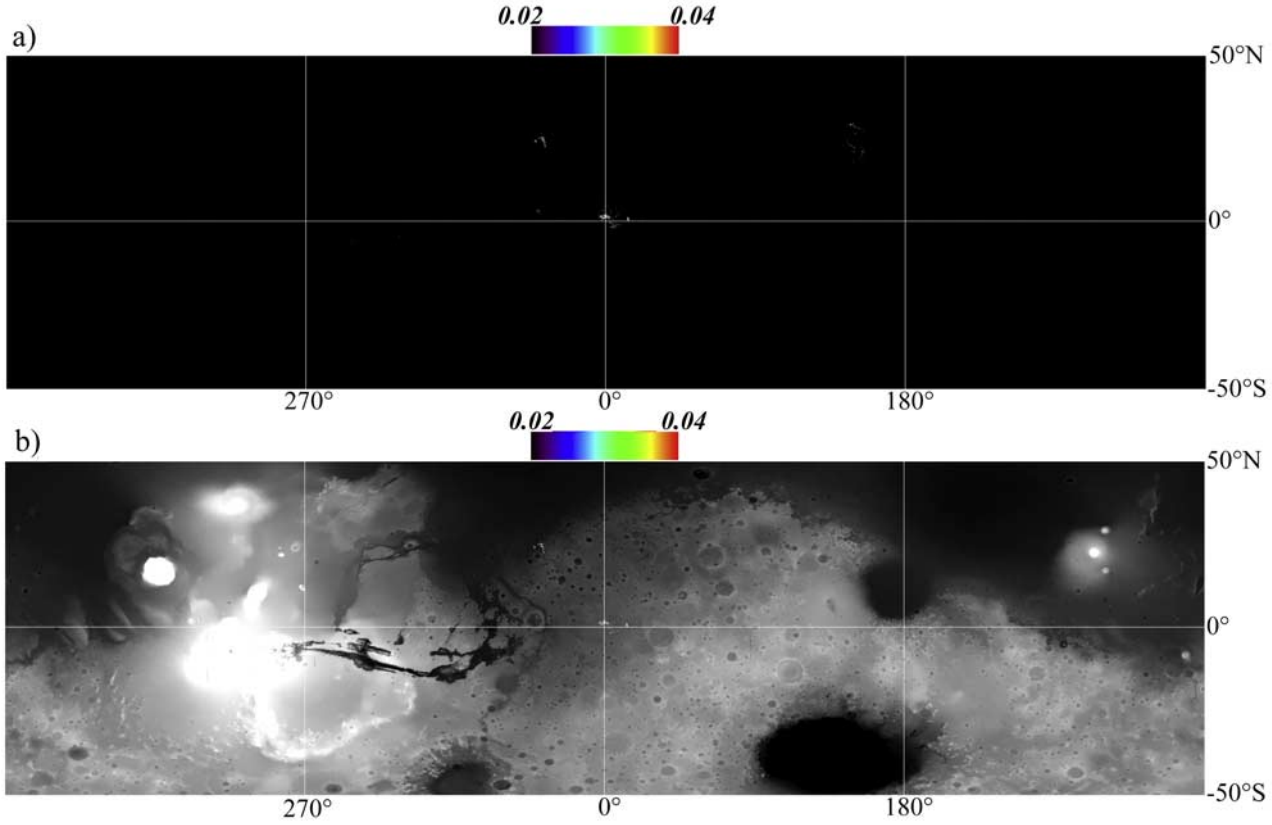

Figure 10. Same as in Figure 6 but for the hydrated minerals identified with the 1.9-μm band criterion.

spatial correlation exists between the dust distribution derived from *Ruff and Christensen* [2002] and the np-Ox distribution, suggesting that the np-Ox map can also serve as an indicator of surface-obscuring dust that can impact spectral measurements.

[41] The chemistry of the surface bright soils derived from in situ measurements is remarkably similar for all landing sites, supporting the idea that the bright dust results from current oxidative weathering and that it is a global unit redistributed by wind [*Yen et al.*, 2005]. The presence of a ferric absorption feature over dark mafic regions (section 5.2) also supports the assumption that the dust has been redistributed (not uniformly) by atmospheric and aeolian processes. Martian dust fall rates of about 20–45 μm per Earth year have been estimated from measurements during the Pathfinder mission [*Johnson et al.*, 2003], but the deposition is expected to be nonuniform at a global scale. A new view of the dust deposition on Mars has been provided by *Newman et al.* [2005] in using the Martian Global Climate Model (MGCM hereafter) simulations with different obliquities of the planet. Their MGCM results indicate that the dust, which has been well mixed within the atmosphere, is deposited preferentially over high topography. For high obliquities with wind stress lifting, the model produces peak net removal within western boundary currents and southern midlatitude bands, and net accumulation concentrated in Tharsis and Arabia [*Newman et al.*, 2005], thus partially explaining the nanophase ferric oxide distribution. On the other hand, the GCM simulations at all obliquities fail to predict peak accumulation over the Amazonis and Elysium regions [*Newman et al.*, 2005], observed to have high "dust" content. This supports the idea that the ferric component could partly result from an in situ nonaqueous alteration of the surface material.

6.2. Mafics

[42] TES spectra have been interpreted as being representative of two general spectral classes: the basaltic type I and the andesitic type II [*Bandfield et al.*, 2000]. On the basis of the present study the distribution of pyroxene-rich materials is in general agreement with the TES type I map. However, the olivine maps resulting from this study provide new insight about the unaltered mafic-rich terrains. Olivine appears to be Mg-rich and mainly mixed with pyroxene. These observations are consistent with recent analysis of THEMIS and TES data that conclude that Fe-olivine is not abundant [*Koeppen and Hamilton*, 2006]. The pyroxene/olivine deposits are detected in diverse terrains such as dunes, crater ejecta, irregular and rough terrains. The rare and small olivine-rich (more iron-rich and larger grain size) deposits are observed in different types of terrains than were discussed by *Mustard et al.* [2005]: small outcrops, isolated massifs, crater floors in addition to the large regional outcrop in Nili Fossae. Additional work is required to study the morphology of these numerous olivine-rich deposits with high-resolution imagery.

[43] It is important to note that the OMEGA and TES data sets are complementary for deriving the mineral abundances of these regions: while OMEGA data are most suitable for detecting and constraining the size of the pyroxene and

olivine grains, TES provides identification of the feldspatic components. In a more general sense, significant new insights are likely to be gained by combining data from the two wavelength regions, enabling well resolved mineral identifications and providing estimates of abundances.

6.3. Northern Low-Albedo Regions

[44] Several hypotheses have been presented to explain the apparent andesitic character of the Acidalia-type spectrum: weathering of basalt to produce clay minerals [*Wyatt and McSween*, 2002], silica coating basalt [*Kraft et al.*, 2003], water-bearing minerals such as opaline, silica-rich allophane like mineraloids, and the most silica-rich zeolites [*Michalski et al.*, 2005], oxidation and recrystallisation of a SNC-type basalt [*Minitti et al.*, 2002], palagonization of basalt [*Morris et al.*, 2003], oxidation at high temperature of a glass-rich basalt flows [*Minitti et al.*, 2005]. These proposed mineralogies and implied origins offer broad possibilities for processes of formation. OMEGA observations show unique spectral attributes: very weak basaltic signature, strong blue slope in the NIR and lack of the hydration band at 1.9 μm. The lack of hydration band helps discriminate between the previously proposed compositions. Clays that exhibit significant 1.9-μm feature associated with metal-OH bands in the 2.1–2.5-μm wavelength region should be excluded. This is in agreement with a recent reassessment of the TES data [*Michalski et al.*, 2005]. Since water processing is required to form silica coatings, silica-coated basalt would be expected to exhibit significant water molecular bands, as confirmed by USGS laboratory spectra [*Clark et al.*, 1993]. Therefore silica-coated basalts as well as water-bearing minerals such as opaline, silica-rich allophane like mineraloids, and the most silica-rich zeolites also proposed as putative candidates [*Michalski et al.*, 2005] are not consistent with the OMEGA results. The NIR and thermal spectral properties of oxidized, partially crystalline SNC-based basaltic materials measured in the laboratory are in general not consistent with the spectrally blue materials contained in these dark regions, as has been assessed by a later reanalysis of the spectral properties of oxidized, Martian meteorite-like basalts [*Hamilton and Minitti*, 2003]. Finally, the andesitic composition and the resulting large proportion of high-Si obsidian glass necessary to reproduce the TES spectra is also problematic. Although some crystallization conditions that would yield dry, high-SiO_2 glass can be conceived, the obsidian that is the result of volcanic lava coming in contact with water should be identified by a 1.9-μm water absorption band in the OMEGA spectra.

[45] As mentioned previously, another model to explain Si-rich minerals could be a palagonization of basalt [*Morris et al.*, 2003] or similarly partial weathering of surface type I rocks [*McSween et al.*, 2003]. Actually, OMEGA spectra and observations of thin coatings of iron oxides on a dark (i.e., basaltic) substrate are spectrally similar [*Singer and Roush*, 1983]. At shorter wavelengths, the brighter coating is optically thick keeping albedo high, while at longer wavelength it becomes increasingly transparent so that the basaltic substrate becomes spectrally dominant. If surfaces of dark material are moderately weathered in the form of a thin varnish of ferric oxide-bearing rinds, this would produce this "blue" NIR continuum slope without water band at 1.9 μm. Another very interesting process that produces an anhydrous, ferric coating over a glass-rich basaltic substrate consists in an oxidation of a basaltic substrate at high temperatures (700° and 900°C) in air and CO_2 [*Minitti et al.*, 2005]. This process can be also considered as possible.

[46] However, an alternative origin can be also proposed. Occurrences of materials showing the same spectral characteristics of type II material have been found in the floor of some craters located in the equatorial region. Dark impact glasses have a typical blue slope with no mafic absorption band [*Schultz and Mustard*, 2004]. Therefore this dark material could imply the presence of impact melts or glasses. This would support the assumption that deposits of impact melts and glasses produced by major impacts since the late Hesperian could provide an alternative interpretation for surface composition type II spectra [*Schultz and Mustard*, 2004].

6.4. Hydrated Minerals

[47] The water-bearing minerals identified by the 1.9-μm spectral criterion are locally in restricted sites at the surface of Mars. The implications of these detections of major importance to trace the past environment are still under investigation, but the major trends have been stated [*Bibring et al.*, 2006]: a first *phyllocian* period (formation of phyllosilicates) indicating an aqueous alteration very early in its history, followed by a *theeikian* phase during which sulfates were formed in an acidic environment.

7. Conclusion

[48] The global maps summarized in this work confirm the general trends of the distribution of surface material at Mars. The low-albedo regions have a pyroxene-rich composition; the bright regions are spectrally comparable to anhydrous nanophase ferric oxides. A comparison of the global "dust" global distribution with the past and present dust activities simulated with GCM indicates that large parts of the bright regions (Amazonis and Elysium) should not be covered by such a ferric component. It is therefore proposed that this ferric material may be not only a large-scale mobile component, but could partly result from in situ alteration. Olivine is identified in large areas associated with low-albedo pyroxene-rich highlands. Values of the olivine spectral indexes indicate that olivine is dominantly Mg-rich with grain size distribution likely less than 100 μm. The detection limit of olivine depends on the grain size. Mg-rich olivine as fine grains (10 μm in size typically) could be widely distributed in the pyroxene-rich terrains at abundance <20%, and not detected spectrally. By contrast, deposits containing coarse grain size distribution of forsterite, and/or more iron-rich forsterite at many grain sizes, can be detected in localized areas. Our best model to explain the VNIR spectral properties of the northern regions is that thin ferric coating or varnish is present on dark basaltic substrate. Such a composition could be consistent with TES observations. Finally, hydrated minerals have been detected in a variety of spatially restricted and highly specific areas.

[49] The next step of our analysis will consist of (1) retrieving abundances and assessing physical parameters such as mean grain size distribution for each mineral, through nonlinear deconvolution [*Poulet and Erard*, 2004],

and (2) initiating a systematic study using OMEGA results to complement those of thermal instruments, MGS/TES, and Odyssey/THEMIS, sensitive to non-Fe-bearing minerals such as plagioclase.

[50] **Acknowledgments.** At the time of this writing (beginning 2007), OMEGA is in excellent health and still targeting the surface of Mars. Its performance and longevity are testimony to the efforts of talented and dedicated engineers and scientists who made the ESA/Mars Express mission and the OMEGA instrument possible. We would also like to thank Michelle Minitti and an anonymous reviewer for thorough and insightful reviews. This work was partially supported by the CNES.

References

Arvidson, R. E., F. Poulet, J.-P. Bibring, M. Wolff, A. Gendrin, R. V. Morris, J. J. Freeman, Y. Langevin, N. Mangold, and G. Bellucci (2005), Spectral reflectance and morphologic correlations in Eastern Terra Meridiani, Mars, *Science*, *307*, 1591–1594, doi:10.1126/science.1109509.

Bandfield, J. L. (2002), Global mineral distributions on Mars, *J. Geophys. Res.*, *107*(E6), 5042, doi:10.1029/2001JE001510.

Bandfield, J. L., V. E. Hamilton, and P. R. Christensen (2000), A global view of Martian surface compositions from MGS-TES, *Science*, *287*, 1626–1630.

Bell, J. F., III (1992), Charge-coupled device imaging spectroscopy of Mars 2: Results and implications for Martian ferric mineralogy, *Icarus*, *100*, 575–597.

Bell, J. F., III, R. V. Morris, and J. B. Adams (1993), Thermally altered palagonitic tephra: A spectral and process analog to the soil and dust of Mars, *J. Geophys. Res.*, *98*, 3373–3385.

Bell, J. F., III, et al. (2000). Mineralogic and compositional properties of Martian soil and dust: Results from Mars Pathfinder, *J. Geophys. Res.*, *105*, 1721–1756.

Bellucci, G., F. Altieri, J.-P. Bibring, G. Bonello, Y. Langevin, B. Gondet, and F. Poulet (2006), OMEGA/Mars Express: Visual channel performances and data reduction techniques, *Planet. Space Sci.*, *54*, 675–684, doi:10.1016/j.pss.2006.03.006.

Bibring, J.-P., et al. (2004) OMEGA: Observatoire pour le Minéralogie, l'Eau, les Glaces et l'Activité, *Eur. Space Agency Spec. Publ.*, *ESA SP 1240*, 37–49.

Bibring, J.-P., et al. (2005), Mars surface diversity as revealed by the OMEGA/Mars Express observations, *Science*, *307*, 1576–1581, doi:10.1126/science.1109509.

Bibring, J.-P., Y. Langevin, J. Mustard, F. Poulet, R. E. Arvidson, A. Gendrin, B. Gondet, N. Mangold, P. Pinet, and F. Forget (2006), Global mineralogical and aqueous Mars history derived from OMEGA/Mars Express data, *Science*, *312*, 400–404, doi:10.1126/science.1122659.

Bishop, J. L., C. M. Pieters, R. G. Burns, J. O. Edwards, R. L. Mancinelli, and H. Froeschl (1995), Reflectance spectroscopy of ferric sulfate-bearing montmorillonites as Mars soil analog materials, *Icarus*, *117*, 101–119.

Bonello, G., J.-P. Bibring, A. Soufflot, Y. Langevin, B. Gondet, M. Berthé, and C. Carabetian (2005), The ground calibration setup of OMEGA and VIRTIS experiments: Description and performances, *Planet. Space Sci.*, *53*, 711–728.

Christensen, P. R., et al. (1998), Results from the Mars Global Surveyor Thermal Emission Spectrometer investigation, *Science*, *279*, 1692–1698.

Christensen, P. R., J. L. Bandfield, M. D. Smith, V. E. Hamilton, and R. N. Clark (2000), Identification of a basaltic component on the Martian surface from Thermal Emission Spectrometer data, *J. Geophys. Res.*, *105*, 9609–9621.

Christensen, P. R., et al. (2003), Morphology and composition of the surface of Mars: Mars Odyssey THEMIS results, *Science*, *300*, 2056–2061.

Christensen, P. R., et al. (2005), Evidence for igneous diversity and magmatic evolution on Mars from infrared spectral observations, *Nature*, *436*, 504–509.

Clark, R. N., and P. G. Lucey (1984), Spectral properties of ice-particulate mixtures and implications for remote sensing: 1. Intimate mixtures, *J. Geophys. Res.*, *89*, 6341–6348.

Clark, R. N., G. A. Swayze, A. J. Gallagher, T. V. V. King, and W. M. Calvin (1993), The Geological U.S. Survey, Digital Spectral Library: Version 1 (0.2 to 3.0μm), *U.S. Geol. Surv. Open File Rep.*, *93–592*, 1340 pp. (Available at http://speclab.cr.usgs.gov/spectral.lib04/clark1993/spectral_lib.html.)

Cloutis, E. A., et al. (2006), Detection and discrimination of sulfate minerals using reflectance spectroscopy, *Icarus*, *184*, 121–157.

Cooper, C. D., and J. F. Mustard (1999), Effects of very fine particle size on reflectance spectra of smectite and palagonitic soil, *Icarus*, *142*, 557–570.

De Grenier, M., and P. Pinet (1995), Near opposition Martian limb-darkening: Quantification and implication for visible near infrared bidirectional reflectance studies, *Icarus*, *115*, 354–368.

Farrand, W. H., J. F. Bell III, J. R. Johnson, S. W. Squyres, J. Soderblom, and D. W. Ming (2006), Spectral variability among rocks in visible and near-infrared multispectral Pancam data collected at Gusev crater: Examinations using spectral mixture analysis and related techniques, *J. Geophys. Res.*, *111*, E02S15, doi:10.1029/2005JE002495.

Fischer, E. M., and C. M. Pieters (1993), The continuum slope of Mars: Bidirectional reflectance investigations and applications to Olympus Mons, *Icarus*, *102*, 185–202.

Gaffey, S. J., L. A. McFadden, D. Nash, and C. Pieters (1993), Ultraviolet, visible and near-infrared reflectance spectroscopy: Laboratory spectra of geologic materials, in *Remote Geochemical Analysis: Elemental and Mineralogical Composition*, edited by C. Pieters and P. A. J. Englert, pp. 43–77, Cambridge Univ. Press, New York.

Gendrin, A., et al. (2005), Sulfates in Martian layered terrains: The OMEGA/Mars Express view, *Science*, *307*, 1587–1591, doi:10.1126/science.1109509.

Gondet, B., J.-P. Bibring, Y. Langevin, F. Poulet, F. Montmessin, and F. Forget (2006), One Martian year observation of H_2O ice clouds by OMEGA/Mars Express, in *Second Workshop on Mars Atmosphere Modelling and Observations*, edited by F. Forget et al., p. 251, Eur. Space Agency, Granada, Spain.

Hamilton, V. E., and P. R. Christensen (2005), Evidence for extensive, olivine-rich bedrock on Mars, *Geology*, *33*, 433–436.

Hamilton, V. E., and M. E. Minitti (2003), Are oxidized shergottite-like basalts an alternative to "andesite" on Mars?, *Geophys. Res. Lett.*, *30*(18), 1915, doi:10.1029/2003GL017839.

Hapke, B. (1993), *Theory of Reflectance and Emittance Spectroscopy*, Cambridge Univ. Press, New York.

Harloff, J., and G. Arnold (2001), Near-infrared reflectance spectroscopy of bulk analog materials for planetary crust, *Planet. Space Sci.*, *49*, 191–211.

Hoefen, T. M., R. N. Clark, J. L. Bandfield, M. D. Smith, J. C. Pearl, and P. R. Christensen (2003), Discovery of olivine in the Nili Fossae region of Mars, *Science*, *302*, 627–630.

Johnson, J. R., and W. M. Grundy (2001), Visible/near-infrared spectra and two layer modeling of palagonite-coated basalts, *Geophys. Res. Lett.*, *28*, 2101–2104.

Johnson, J. R., W. M. Grundy, and M. T. Lemmon (2003), Dust deposition at the Mars Pathfinder landing site: Observations and modeling of visible/near infrared spectra, *Icarus*, *163*, 330–346.

Klingelhöfer, G., et al. (2004), Jarosite and hematite at Meridiani Planum from the Mössbauer spectrometer on the Opportunity rover, *Science*, *306*, 1740–1745.

Koeppen, W. C., and V. E. Hamilton (2006), The distribution and composition of olivine on Mars, *Lunar Planet. Sci. [CD-ROM]*, *XXXVII*, Abstract 1964.

Kraft, M. D., J. R. Michalski, and T. G. Sharp (2003), Effects of pure silica coatings on thermal emission spectra of basaltic rocks: Considerations for Martian surface mineralogy, *Geophys. Res. Lett.*, *30*(24), 2288, doi:10.1029/2003GL018848.

Langevin, Y., F. Poulet, J.-P. Bibring, and B. Gondet (2005a), Sulfates in the north polar region of Mars detected by OMEGA/Mars Express, *Science*, *307*, 1584–1586.

Langevin, Y., F. Poulet, J.-P. Bibring, B. Schmitt, S. Douté, and B. Gondet (2005b), Summer evolution of the north polar cap of Mars as observed by OMEGA/Mars Express, *Science*, *307*, 1581–1584.

Langevin, Y., J.-P. Bibring, F. Montmessin, F. Forget, M. Vincendon, S. Douté, F. Poulet, and B. Gondet (2007), Observations of the south seasonal cap of Mars during recession in 2004–2006 by the OMEGA visible/near-infrared imaging spectrometer on board Mars Express, *J. Geophys. Res.*, doi:10.1029/2006JE002841, in press.

Loizeau, D., et al. (2007), Phyllosilicates in the Mawrth Vallis region of Mars, *J. Geophys. Res.*, doi:10.1029/2006JE002877, in press.

Mangold, N., et al. (2007), Mineralogy of the Nili Fossae region with OMEGA/Mars Express data: 2. Aqueous alteration of the crust, *J. Geophys. Res.*, doi:10.1029/2006JE002835, in press.

McSween, H. Y., Jr., T. L. Grove, and M. B. Wyatt (2003), Constraints on the composition and petrogenesis of the Martian crust, *J. Geophys. Res.*, *108*(E12), 5135, doi:10.1029/2003JE002175.

McSween, H. Y., Jr., et al. (2006), Characterization and petrologic interpretation of olivine-rich basalts at Gusev Crater, Mars, *J. Geophys. Res.*, *111*, E02S10, doi:10.1029/2005JE002477.

Mellon, M. T., B. M. Jakosky, H. H. Kieffer, and P. R. Christensen (2000), High resolution thermal inertia mapping from the Mars Global Surveyor Thermal Emission Spectrometer, *Icarus*, *148*, 437–455.

Michalski, J. R., M. D. Kraft, T. G. Sharp, L. B. Williams, and P. R. Christensen (2005), Mineralogical constraints on the high-silica Martian surface component observed by TES, *Icarus*, *174*, 161–177.

Minitti, M. E., J. F. Mustard, and M. J. Rutherford (2002), Effects of glass content and oxidation on the spectra of SNC-like basalts: Applications to Mars remote sensing, *J. Geophys. Res.*, *107*(E5), 5030, doi:10.1029/2001JE001518.

Minitti, M. E., M. D. Lane, and J. L. Bishop (2005), A new hematite formationon Mars, *Meteoritics Planet Sci.*, *40*, 55–69.

Morris, R. V., D. G. Agresti, H. V. Lauer Jr., J. A. Newcomb, T. D. Shelfer, and A. V. Murali (1989), Evidence for pigmentary hematite on Mars based on optical, magnetic, and Mössbauer studies of superparamagnetic (nanocrystalline) hematite, *J. Geophys. Res.*, *94*, 2760–2778.

Morris, R. V., D. C. Golden, J. F. Bell III, H. V. Lauer Jr., and J. B. Adams (1993), Pigmenting agents in Martian soils: Inferences from spectral, Mössbauer, and magnetic properties of nanophase and other iron oxides in Hawaiian palagonitic soil PN-9, *Geochim. Cosmochim. Acta*, *57*, 4597–4609.

Morris, R. V., D. C. Golden, and J. F. Bell III (1997), Low-temperature reflectivity spectra of red hematite and the color of Mars, *J. Geophys. Res.*, *102*, 9125–9134.

Morris, R. V., et al. (2000), Mineralogy, composition, and alteration of Mars Pathfinder rocks and soils: Evidence from multispectral, elemental, and magnetic data on terrestrial analogue, SNC meteorite, and Pathfinder samples, *J. Geophys. Res.*, *105*, 1757–1817.

Morris, R. V., T. G. Graff, S. A. Mertzman, M. D. Lane, and P. R. Christensen (2003), Palagonitic (not andesitic) Mars: Evidence from thermal emission and VNIR spectra of palagonitic alteration rinds on basaltic rock, paper presented at Sixth International Conference on Mars, Lunar and Planet. Inst., Pasadena, Calif.

Morris, R. V., et al. (2004), Moessbauer mineralogy on Mars: First results from the Spirit landing site in Gusev Crater, *Science*, *305*, 833–836.

Morris, R. V., et al. (2006), Mössbauer mineralogy of rock, soil, and dust at Gusev Crater, Mars: Spirit's journey through weakly altered olivine basalt on the plains and pervasively altered basalt in the Columbia Hills, *J. Geophys. Res.*, *111*, E02S13, doi:10.1029/2005JE002584.

Murchie, S., L. Kirkland, S. Erard, J. Mustard, and M. Robinson (2000), Near-infrared spectral variations of Martian surface materials from ISM imaging spectrometer data, *Icarus*, *147*, 444–471.

Mustard, J. F., F. Poulet, A. Gendrin, J.-P. Bibring, Y. Langevin, B. Gondet, N. Mangold, G. Bellucci, and F. Altieri (2005), Olivine and pyroxene diversity in the crust of Mars, *Science*, *307*, 1594–1597, doi:10.1126/science.1109509.

Newman, C. E., S. R. Lewis, and P. L. Read (2005), The atmospheric circulation and dust activity in different orbital epochs on Mars, *Icarus*, *174*, 135–160, doi:10.1016/j.icarus.2004.10.023.

Pinet, P., and S. Chevrel (1990), Spectral identification of geological units on the surface of Mars related to the presence of silicates from earthbased near-infrared telescopic CCD imaging, *J. Geophys. Res.*, *95*, 14,435–14,446.

Pinet, P., et al. (2006) Detection and regional mapping of mafic minerals across Syrtis Major from OMEGA/Mars Express observations in the visible-near infrared domain by means of MGM deconvolution, paper presented at European Planetary Science Congress 2006, Eur. Planet. Network, Berlin.

Poulet, F., and S. Erard (2004), Nonlinear spectral mixing: Quantitative analysis of laboratory mineral mixtures, *J. Geophys. Res.*, *109*, E02009, doi:10.1029/2003JE002179.

Poulet, F., J.-P. Bibring, J. F. Mustard, A. Gendrin, N. Mangold, Y. Langevin, R. E. Arvidson, B. Gondet, and C. Gomez (2005), Phyllosilicates on Mars and implications for early Martian climate, *Nature*, *438*, 623–628.

Presley, M. A., and P. R. Christensen (1997), Thermal conductivity measurements of particulate materials: 2. Results, *J. Geophys. Res.*, *102*, 6551–6566.

Roush, T. L., F. Esposito, G. R. Rossman, and L. Colangeli (2006), Gypsum optical constants in the visible and near-infrared: Real and imagined, *Lunar Planet. Sci. [CD-ROM]*, 1188.

Ruff, S. W. (2004), Spectral evidence for zeolite in the dust on Mars, *Icarus*, *168*, 131–143.

Ruff, S. W., and P. R. Christensen (2002), Bright and dark regions on Mars: Particle size and mineralogical characteristics based on Thermal Emission Spectrometer data, *J. Geophys. Res.*, *107*(E12), 5127, doi:10.1029/2001JE001580.

Schultz, P. H., and J. F. Mustard (2004), Impact melts and glasses on Mars, *J. Geophys. Res.*, *109*, E01001, doi:10.1029/2002JE002025.

Shkuratov, Y., L. Starukhina, H. Hoffmann, and G. Arnold (1999), A model of spectral albedo of particulate surfaces: Implications for optical properties of the moon, *Icarus*, *137*, 235–246.

Singer, R. B., and T. B. McCord (1979), Mars: large scale mixing of bright and dark materials and properties of dark material, *Proc. Lunar Planet. Sci. Conf.*, *10*, 1128–1130.

Singer, R. B., and T. R. Roush (1983), Spectral reflectance properties of particulate weathered coatings on rocks: Laboratory modeling and applicability to Mars, *Proc. Lunar Planet. Sci. Conf.*, *14*, 708–709.

Squyres, S. W., et al. (2004), The opportunity Rover's Athena Science Investigation at Meridiani Planum, Mars, *Science*, *306*, 1698–1703, doi:10.1126/science.1106171.

Wells, E. N., J. Veverka, and P. Thomas (1984), Mars: Experimental study of albedo changes caused by dust fallout, *Icarus*, *587*, 331–338.

Wyatt, M. B., and H. Y. McSween (2002), Spectral evidence for weathered basalt as an alternative to andesite in the Martian lowlands of Mars, *Nature*, *417*, 263–266.

Yen, A. S., et al. (2005), An integrated view of the chemistry and mineralogy of Martian soils, *Nature*, *436*, 49–54, doi:10.1038/nature03637.

G. Belluci, Istituto Nazionale Di Astrofiscia dello Spazio Interplanetario, Rome, I-00133 Italy.

J.-P. Bibring, C. Gomez, B. Gondet, Y. Langevin, and F. Poulet, Institut d'Astrophysique Spatiale, CNRS/Université Paris-Sud, Orsay Cedex, F-91405 France. (francois.poulet@ias.fr)

J. Mustard, Geological Sciences, Brown University, Providence, RI 02912, USA.

P. Pinet, DTP/UMR5562, CNRS, Toulouse, F-31400 France.